

Three-dimensional time-dependent Hartree-Fock calculations: Application to $^{16}\text{O} + ^{16}\text{O}$ collisions*

H. Flocard[†]

Nuclear Science Division, Lawrence Berkeley Laboratory, University of California, Berkeley, California 94720

S. E. Koonin[‡]

W. K. Kellogg Radiation Laboratory, California Institute of Technology, Pasadena, California 91125

M. S. Weiss[§]

Lawrence Livermore Laboratory, University of California, Livermore, California 94550

(Received 22 November 1977)

A coordinate-space method is developed to solve the three-dimensional time-dependent Hartree-Fock equations. It is applied to the study of $^{16}\text{O} + ^{16}\text{O}$ collisions at $E_{\text{lab}} = 105$ MeV for incident angular momenta from 0 to $40\hbar$. We find fusion for $L = 13\hbar$ through $27\hbar$ and highly inelastic scattering for $L \leq 12\hbar$.

[NUCLEAR REACTIONS $^{16}\text{O}(^{16}\text{O}, x)$ in three-dimensional time-dependent Hartree-Fock approximation. Fusion and strongly damped collisions.]

I. INTRODUCTION

Time-dependent Hartree-Fock theory¹ (TDHF) has emerged in recent years as a promising candidate for a tractable microscopic theory of large-amplitude collective motion. Although investigations of TDHF's theoretical content date from the last decade,^{2,3} current interest in the method is due largely to the realization that it might adequately describe heavy-ion reactions and fission.⁴⁻⁸ The first application of TDHF to reaction phenomena was made by Bonche, Koonin, and Negele,⁹ who numerically studied the one-dimensional collision of slabs of nuclear matter. This work was followed by the studies of Cusson and Maruhn for $^{12}\text{C} + ^{12}\text{C}$ (Ref. 10), and by those of Koonin¹¹ and Koonin *et al.*¹² for $^{16}\text{O} + ^{16}\text{O}$ and $^{40}\text{Ca} + ^{40}\text{Ca}$. These calculations were two-dimensional in the sense of treating axially symmetric three-dimensional systems. In the latter paper some effects of finite impact parameters were accounted for by a phenomenological rotating frame approximation. The axially symmetric work has been extended to the mass-asymmetric system $^{14}\text{N} + ^{12}\text{C}$ by Maruhn-Rezwani, Davies, and Koonin.¹³ Some truly two-dimensional calculations of the collisions of disks of nuclear matter which allow for axial asymmetries have been performed by Bonche *et al.*¹⁴ Fully three-dimensional calculations were first reported by Cusson, Smith, and Maruhn,¹⁵ who studied some collisions of $^{16}\text{O} + ^{16}\text{O}$ using a zero-range effective interaction, and then included the Coulomb force in a more extensive series of calculations which treated the $^{14}\text{N} + ^{12}\text{C}$ system as well.¹⁶ Detailed reviews of much

of this activity have been given by Kerman¹⁷ and Bonche.¹⁸

In this work we present a technique for solving the TDHF equations in three dimensions (3D) and demonstrate its application by an extensive study of the $^{16}\text{O} + ^{16}\text{O}$ system at $E_{\text{lab}} = 105$ MeV. Our study is complementary to that of Bonche, Grammaticos, and Koonin¹⁹ who have explored many energies at a limited number of impact parameters in order to determine the fusion excitation function. We feel it is important to do these calculations in 3D so as to eliminate the necessity of assumptions other than the TDHF approximation.

Our calculations have been motivated by several considerations. At the most practical level, the nonlinear nature of the TDHF equations makes analytic study impossible and numerical calculations essential. Our understanding is still at the stage of asking questions about what the TDHF equations "do." The calculations presented here impose a minimum of constraints on the symmetry of the TDHF determinant and so begin to give answers to these questions which are free from the uncertainties due to simplified geometries. They are also stringent tests of the validity of the simpler two-dimensional calculations. At the phenomenological level, TDHF has the appeal of naturally extending the shell model to dynamical problems. As a result, phenomenological models of heavy-ion reactions such as the liquid drop model²⁰ and the one-body viscosity²¹ can be related to the independent particle picture realized in the Hartree-Fock (HF) and TDHF approaches. These are also natural analogies between TDHF and a fluid dynamical picture.^{22,23} Our results

help us to understand these connections. Finally, at a fundamental level, many aspects of TDHF remain unclear. Some results have been obtained in connection with the translational invariance,² rotational invariance,³ and continuity equations^{8,24} of the theory and both the small amplitude [random phase approximation (RPA)] and adiabatic⁴⁻⁷ limits have been related to ordinary quantum mechanics. However, the interpretation of the results of the general theory remains vague and has been limited almost exclusively to the most naive classical picture. In particular, a precise understanding of the relationship between the TDHF initial conditions and the Schrödinger wave packet used in ordinary time-dependent collision theories²⁵ is still missing. Quantal and classical aspects are intertwined in a way such that it is difficult to determine the predictive powers of the theory. However, our complete comprehension does not mean that contact with experiment is not possible, but only that we do not know how to fully extract the information contained in our results.

The remainder of the paper is organized as follows: In Sec. II we review the basic TDHF equations and present the effective interaction we have used. The symmetries imposed on the TDHF determinant for computational reasons are treated in Sec. III. Section IV presents the initial conditions and Sec. V contains our results. Section VI is a discussion of the results, and Sec. VII is our conclusion. The technical details of our calculations are contained in the Appendixes. Appendix A is concerned with the numerical discretization of the TDHF energy functional and its effect on the translational invariance properties of the finite difference equations. In Appendix B we discuss several methods for evolving the three-dimensional TDHF equations with a finite time step. Finally, Appendix C contains a discussion of a method for solving the discrete Poisson and Helmholtz equations which are necessary for obtaining the one-body Coulomb and Yukawa potentials.

II. TDHF EQUATIONS

A detailed discussion of the TDHF theory can be found in many papers.^{1-9,12,13} For completeness, we will only outline the derivation of the equations here.

In the TDHF approximation, the many-body wave function of an A -nucleon system is constrained at all times to be a single Slater determinant Ψ . The equations governing the evolution of the associated orthonormal single-particle (s.p.) wave functions $\{\psi_j, j=1, \dots, A\}$ can be derived from a variational principle which makes the "action"

$$\mathcal{J} = \int_{t_1}^{t_2} dt \langle \Psi(t) | i\hbar \frac{\partial}{\partial t} - \hat{H} | \Psi(t) \rangle \quad (1)$$

stationary with respect to the variation of these wave functions.^{6,7} Here, \hat{H} is the many-body Hamiltonian operator, which in practice is taken to be the kinetic energy and a two-body effective interaction. The variation of Eq. (1) then leads to the coupled TDHF equations

$$i\hbar \frac{\partial \psi_j}{\partial t} = h(t)\psi_j, \quad j=1, \dots, A, \quad (2)$$

where h is the time-dependent Hermitian one-body HF Hamiltonian. A nonlinear coupling among the equations (2) arises from the functional dependence of h upon the $\{\psi_j\}$. As a consequence, the superposition principle does not hold for these equations. Two important properties of the TDHF equations are the conservation of the total energy

$$E = \langle \Psi(t) | \hat{H} | \Psi(t) \rangle, \quad (3)$$

which follows directly from the variational formulation of the theory, and the time independence of the inner products of the $\{\psi_j\}$ among themselves.

The most general expressions for E and h in terms of \hat{H} can be found in Refs. 3-6. We shall henceforth consider only the effective interaction used in our work and follow Ref. 12 in writing the total energy as a functional of the nucleon density

$$\rho(\vec{r}) = \sum_{j=1}^A |\psi_j(\vec{r})|^2 \quad (4)$$

and the kinetic energy density

$$\tau(\vec{r}) = \sum_{j=1}^A |\vec{\nabla} \psi_j(\vec{r})|^2, \quad (5)$$

$$E = \int d\vec{r} \left[\frac{\hbar^2}{2m} \tau + \frac{3}{8} t_0 \rho^2 + \frac{1}{16} t_3 \rho^3 \right] + \frac{1}{2} V_0 \int d\vec{r} \int d\vec{r}' \rho(\vec{r}) \frac{\exp(-|\vec{r} - \vec{r}'|/a)}{|\vec{r} - \vec{r}'|/a} \rho(\vec{r}') + \frac{1}{2} e^2 \int d\vec{r} \int d\vec{r}' \rho_p(\vec{r}) \frac{1}{|\vec{r} - \vec{r}'|} \rho_p(\vec{r}'). \quad (6)$$

The first term in the brackets is the kinetic energy, while the following two terms are the expectation value of the zero-range density-dependent two-body effective interaction

$$t_0 \delta(\vec{r}_1 - \vec{r}_2) + \frac{t_3}{6} \rho \left(\frac{\vec{r}_1 + \vec{r}_2}{2} \right) \delta(\vec{r}_1 - \vec{r}_2). \quad (7)$$

The last two terms in Eq. (6) are the expectation values of a Yukawa interaction and the direct Coulomb interaction [ρ_p is the proton density defined similarly to Eq. (4)].

The functional variation of the energy E , as depicted in Eq. (6), with respect to the $\{\psi_j^*\}$ leads di-

TABLE I. Values of the coefficients of the Skyrme and Yukawa interactions.

t_0 (MeV fm ³)	t_3 (MeV fm ⁶)	V_0 (MeV)	a (fm)
-497.66	172.88	-363.044	0.4598

rectly to the TDHF one-body Hamiltonian

$$h = -\frac{\hbar^2}{2m}\nabla^2 + \frac{3}{4}t_0\rho + \frac{3}{16}t_3\rho^2 + W_Y + W_C. \quad (8a)$$

Here, the Yukawa potential is

$$W_Y(\vec{r}) = V_0 \int d\vec{r}' \frac{\exp(-|\vec{r} - \vec{r}'|/a)}{|\vec{r} - \vec{r}'|/a} \rho(\vec{r}'), \quad (8b)$$

and the Coulomb potential (which is effective only for protons) is

$$W_C(\vec{r}) = e^2 \int d\vec{r}' \frac{1}{|\vec{r} - \vec{r}'|} \rho_p(\vec{r}'). \quad (8c)$$

Equations (2) and (8) are the TDHF equations we solve by means of the coordinate-space methods outlined in the Appendixes. The parameters t_0 , t_3 , V_0 , and a used in the present paper are those of Ref. 12 and are given in Table I.

III. SYMMETRIES

The history of numerical TDHF calculations has been one of the gradual relaxation of symmetry constraints imposed on the determinantal wave function. Such symmetries have been useful in reducing the magnitude of the numerical effort involved and have therefore allowed basic investigations of the TDHF equations. However, it now seems probable that a full test of the possibilities of the TDHF theory in realistic situations will require the breaking of as many symmetries as is possible. Unfortunately, while we would like to relax as many "built-in" constraints as we can, practical reasons have forced us to retain the four symmetries we discuss below.

In solving the TDHF equations we have assumed a perfect spin-isospin degeneracy, so that each spatial orbital is occupied by four nucleons. In this case, the proton density in Eqs. (6) and (8c) is replaced by one-half of the nucleon density and the Coulomb potential [Eq. (8c)] acts on all spatial orbitals. This imposed degeneracy makes our calculations applicable only to 4- N systems. One- or two-nucleon transfers are not accurately described in our model and nucleon emission is incorrectly accounted for. The isospin degeneracy, which is very accurately conserved in TDHF calculations of light systems which allow for the neutron-pro-

ton degrees of freedom,¹⁰ can easily be removed with an increase of a factor of 2 in computing time and storage. Removal of the spin degeneracy would be more complicated. A spin-orbit interaction demands that each wave function be partially spin-up and spin-down. Therefore, including the spin degree of freedom would increase storage and computation by at least a factor 4.

We have also imposed two spatial symmetries on the TDHF determinant. These are reflection symmetry with respect to the reaction plane (taken to be the $Z=0$ plane) and point reflection symmetry through the center of mass (c.m.) of the total system (taken to be the origin). These symmetries reduce our numerical effort by a factor of 4. In Appendix A we show how they have been implemented practically in our calculations.

Of the two spatial symmetries, the second is probably the more restrictive since it limits the calculations to systems of two identical ions. However, it seems unlikely that mass-asymmetric degrees of freedom would be significant in an unconstrained calculation of the light symmetric systems we consider here. Despite the four symmetries we have imposed, our calculations represent a significant advance over the previous two-dimensional work.¹⁰⁻¹³ As we shall see in Secs. V and VI, the inclusion of triaxial degrees of freedom leads to substantial qualitative effects on the TDHF results, although axial symmetry appears to be an adequate approximation for grazing and nearly head-on collisions. (In terms of the usual β, γ parametrization of triaxial shapes,²⁶ the dynamics of the two-dimensional calculations are restricted to the lines $\gamma=0$ and $\gamma=\frac{1}{3}\pi$, while our three-dimensional calculations cover the entire range $0 \leq \gamma \leq \frac{1}{3}\pi$.) Of course, the effects of the centrifugal force due to finite impact parameters are naturally taken into account in our 3D calculations and we do not have to make any assumptions about the moment of inertia, as is done in Ref. 12.

IV. INITIAL CONDITIONS

The TDHF equations (2) are first order in time, so that the values of all of the single-particle wave functions at some time $t=0$ are required as initial conditions. Since we solve the equations in the overall c.m. frame, these should be chosen to represent identical nuclei approaching one another at a finite impact parameter with equal and opposite velocities $\vec{v} = \pm \hbar \vec{k}/m$. We have therefore constructed the initial state by multiplying each of the single-particle wave functions of the static HF solution of each nucleus by the phase $e^{i\vec{k}\cdot\vec{r}}$. [To find the static HF solutions used in our cal-

culution, we evolve equations similar to (2) and (8), beginning with an arbitrary trial determinant constructed from single-particle orbitals with the required symmetries. The evolution is done on the discrete spatial mesh described in Appendix A, using an evolution method similar to those described in Appendix B with the replacement $\Delta t \rightarrow -i\Delta t$. When the single-particle wave functions are orthonormalized after every "time" step, there is rapid convergence to the ground state solution provided the magnitude of Δt is sufficiently small.] In the absence of numerical inaccuracies (cf. Appendix A) this determinant represents two ^{16}O nuclei which translate uniformly with the required velocities prior to collision. In practice, we start the nuclei along the classical Coulomb trajectory they would have followed from infinity to the relatively large separation we choose at $t=0$ (~ 16 fm). Our initial conditions therefore neglect the demonstrably small effects of Coulomb-induced deformations prior to $t=0$.

Such an initial condition is usually interpreted as a wave packet despite the fact that we have only multiplied the static Slater determinant by the plane wave $\exp(i\vec{k}\cdot\vec{R})$, where $\vec{R}=\sum_{j=1}^A\vec{r}_j$. In fact the wave packet is already contained in the static HF solution, which is not an eigenstate of the total momentum. If we assume that we can factor out the center-of-mass motion we may write

$$\psi_{\text{HF}}(\text{static}) = G(\vec{R})\chi, \quad (9)$$

where $G(\vec{R})$ stands for the wave function of the c.m. and χ for the internal wave function. This is certainly a good approximation for an ^{16}O nucleus. Indeed, the HF single-particle orbitals of light nuclei are very close to oscillator wave functions, for which the factorization is exact. The Fourier transform of $G(\vec{R})$ would be the wave packet in momentum space. The only result achieved by the multiplication by $e^{i\vec{k}\cdot\vec{R}}$ is a shift of the center of momentum of this wave packet by the vector \vec{k} , without any change in its shape. The translating TDHF wave function would then be

$$\psi_{\text{TDHF}}(\text{transl}) \approx \exp\left\{-i\frac{t}{\hbar}\left[\sum_{j=1}^A\left(\epsilon_j + \frac{\hbar^2 k^2}{2m}\right)\right]\right\} \times G(\vec{R} - \vec{v}t)\chi. \quad (10)$$

In Eq. (10), the ϵ_j are the static HF single-particle energies. For a ^{16}O nucleus of oscillator wave functions, the kinetic energy associated with the c.m. motion is $1/24$ of the total kinetic energy. Using this ratio for the static HF wave function we find a spread in energy of about 10 MeV. A direct correspondence of the TDHF wave packet to a Schrödinger wave packet would lead us to con-

clude that 10 MeV gives a measure of the energy resolution of the incident beams associated with each ^{16}O nucleus.

There are, however, several crucial differences between a translating TDHF solution and a Schrödinger wave packet. These come mainly from the restricted variational space (one Slater determinant) used in the theory. We are not free to change arbitrarily the shape of the c.m. wave packet. The static HF equations give at the same time the wave functions for the internal degrees of freedom and for the center of mass. In contrast with the Schrödinger picture, all the degrees of freedom are coupled by the minimization process in the space of the Slater determinants. (One could imagine changing the shape of the HF wave packet by solving the static equations with an external constraint like \vec{P}^2 where \vec{P} is the total momentum. However, this would induce a change in the internal wave function χ .) The same coupling is responsible for the fact that the TDHF wave packet does not spread as a function of time, as does the Schrödinger wave packet (except for the trivial case $A=1$, where the HF and Schrödinger wave packets are identical). In fact, Eq. (10) is identical to formula (15) of Ref. 25 describing a Schrödinger wave packet in the limit where spreading is neglected. In the same reference one finds an expression (formula 19) for a quantity e which should stay small for the spreading of the wave packet to be negligible:

$$e = \frac{1}{w} \left(\frac{\Delta t \hbar}{2wM} \right). \quad (11)$$

Here Δt is the total time during which the wave packet is followed, w is the spatial width of the function $G(\vec{R})$, and M is the total mass of the system. If we use $\Delta t = 10^{-21}$ sec, which corresponds in our calculations to a typical full collision time, then $e = 0.5$ (we take $w = 2$ fm). This number is certainly not negligible, but may be sufficiently small to allow correspondence between the TDHF solution and a Schrödinger wave packet. If we were to adopt this viewpoint, then a quantitative comparison between our results and a normal Schrödinger equation would require an understanding of the evolution of a Schrödinger wave packet with a 10-MeV spread during a collision over times of the order of 10^{-21} sec.

An alternative position one may take is that we are really only interested in following the wave packet for 2×10^{-22} sec, the time for our nuclei to move from their initial position to contact. Then $e = 0.1$ and one does not have to worry about spreading.

In the following we shall mainly interpret our TDHF results from a classical point of view. This

is consistent with the fact that a nonspreading wave packet is the characteristic of a classical particle, as can be seen from the linear dependence of the spreading parameter e on \hbar (11).

V. RESULTS

Our numerical methods provide, at each time step, the set of single-particle wave functions $\psi_j(\vec{r}, t)$, or equivalently, the one-body density matrix. Because this represents far more information than can be comprehended easily, we have elected to display some of the physically relevant quantities derivable from these wave functions.

In Figs. 1–3 we show the nucleon density ρ at various times for collisions with impact parameters corresponding to $L = 40\hbar$, 13, and $5\hbar$. The figures show contour plots of the density integrated along the direction perpendicular to the reaction plane.

For the largest value of the angular momentum ($L = 40\hbar$) the nuclei appear to pass each other without excitation. A comparison with the classical Coulomb trajectory shows that indeed no nuclear interaction takes place and that Coulomb excita-

tion is negligible. Within the precision of our calculation, $L = 40\hbar$ corresponds to the minimum angular momentum for pure Coulomb scattering.

For a smaller value of the angular momentum ($L = 13\hbar$), the collision leads to fusion. The two nuclei remain in contact for a time longer than 3×10^{-21} sec; the time at which we stopped this calculation. Some shapes exhibit strong nonaxial deformations. In fact, the analysis of the quadrupole moment tensor shows that the γ asymmetry angle sometimes reaches values higher than 20° (for $L = 15\hbar$, γ has temporarily exceeded 30°).

At an even smaller impact parameter ($L = 5\hbar$), fusion no longer occurs and two fragments emerge directly after the collision. (The density at the origin does not go back to exactly zero after the separation of the main fragments. It stays within 10^{-3} to 10^{-2} of the density in the center of the outgoing fragments compared to the value 10^{-7} before the collision. We cannot determine whether this is due to some small probability fusion process or to numerical inaccuracies. In the analogous way, when a fusion takes place as with $L = 13\hbar$, the density at the edges of the box gradually rises to a 10^{-3} – 10^2 ratio to the density at the origin,

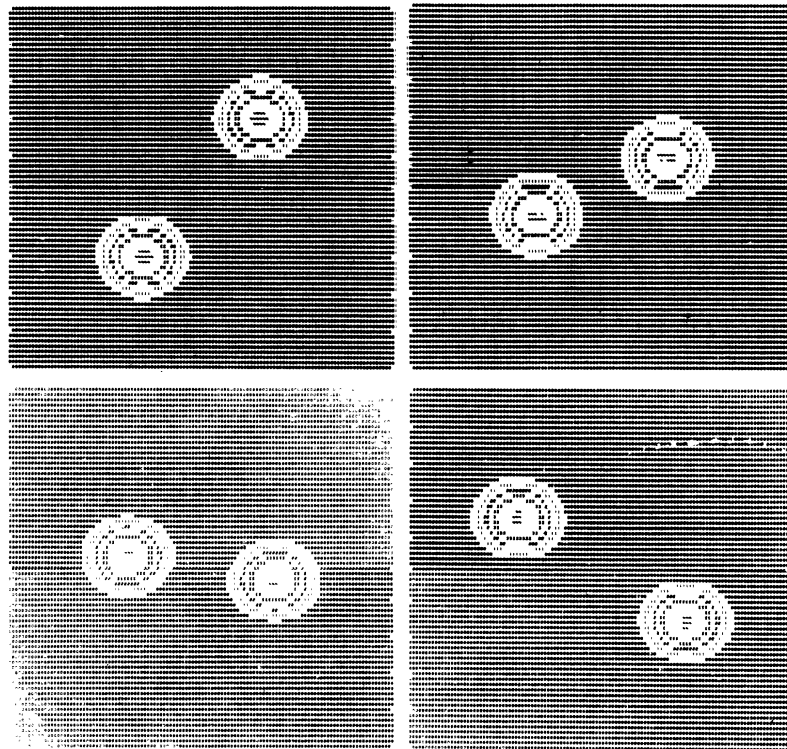


FIG. 1. Contour lines of the density integrated over the coordinate normal to the scattering plane for an $^{16}\text{O}+^{16}\text{O}$ collision at $E_{\text{lab}} = 105$ MeV and incident angular momentum $L = 40\hbar$. The time interval between two pictures is 2×10^{-22} sec.

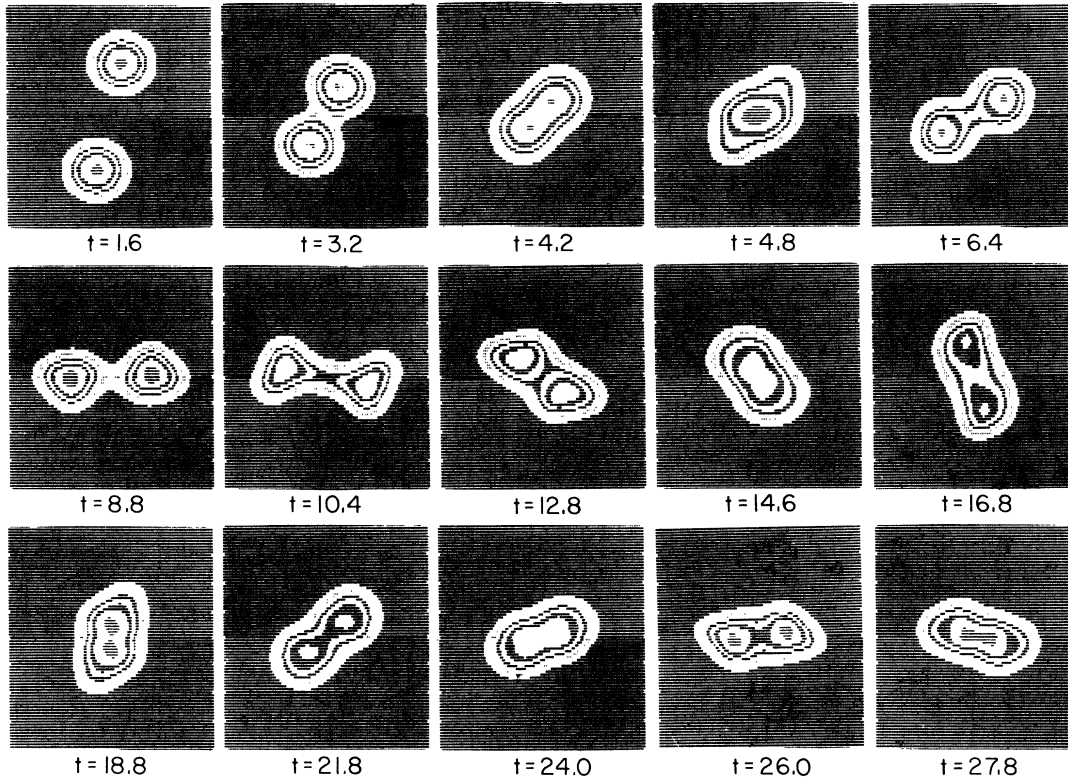


FIG. 2. Contour lines of the density integrated over the coordinate normal to the scattering plane for an $^{16}\text{O} + ^{16}\text{O}$ collision at $E_{\text{lab}} = 105$ MeV and incident angular momentum $L = 13\hbar$. The times t are given in units of 10^{-22} sec.

as if some matter were being radiated out of the fused system.) One must remember that these fragments do not correspond to only ^{16}O nuclei since some transfer has occurred during the reaction.¹² In addition, a large amount of the initial kinetic energy ($\sim 80\%$) has been transferred to internal degrees of freedom, as can be seen in the large octupole oscillations of the fragments after the collision.

A more physical description of the collision process can be obtained by plotting the trajectories of the c.m. of each fragment for different L . However, the reduction of such a complex dynamical system to a single coordinate can lead to some unusual effects, as we discuss below. In addition, there is no unique way to define a fragment and this notion even loses meaning for complete fusion configurations. In this paper we have adopted the following definition. After having determined the principal axes of the inertia tensor of the mass density, we define a fragment as the matter located on one side of the inertial axis associated with the largest eigenvalue and then take its center-of-mass. Another possible prescription is to diagonalize the mass quadrupole tensor and choose

the orientation of the c.m.'s axis as that associated with the largest moment Q ($Q > 0$). The distance R between the c.m.'s of the two ^{16}O is then defined as $R = (Q/A)^{1/2}$, where $A = 16$ in our case. For the results presented here, this definition and the one above lead essentially to the same trajectories. The difference in the angle never exceeds 2° and the difference in distances R is never larger than 0.3 fm. A significant difference would only occur for very compact mass distributions.

In Fig. 4 we have plotted the trajectories of the vector \vec{R} joining the c.m.'s of the fragments for several values of the angular momentum. The trajectories can be divided into three groups. Large values of L ($L > 27\hbar$) do not lead to fusion. As mentioned before, $L \geq 40\hbar$ yields pure Coulomb scattering. The rainbow angular momentum is found around $35\hbar$, and between $L = 33$ and $27\hbar$ the deflection angle becomes negative as the nuclear attraction overcomes the Coulomb repulsion.

The second group of trajectories leads to fusion ($13\hbar \leq L \leq 27\hbar$). Different examples of these are shown separately in Fig. 5. They are qualitatively very different. For the large values of L ($L = 27$

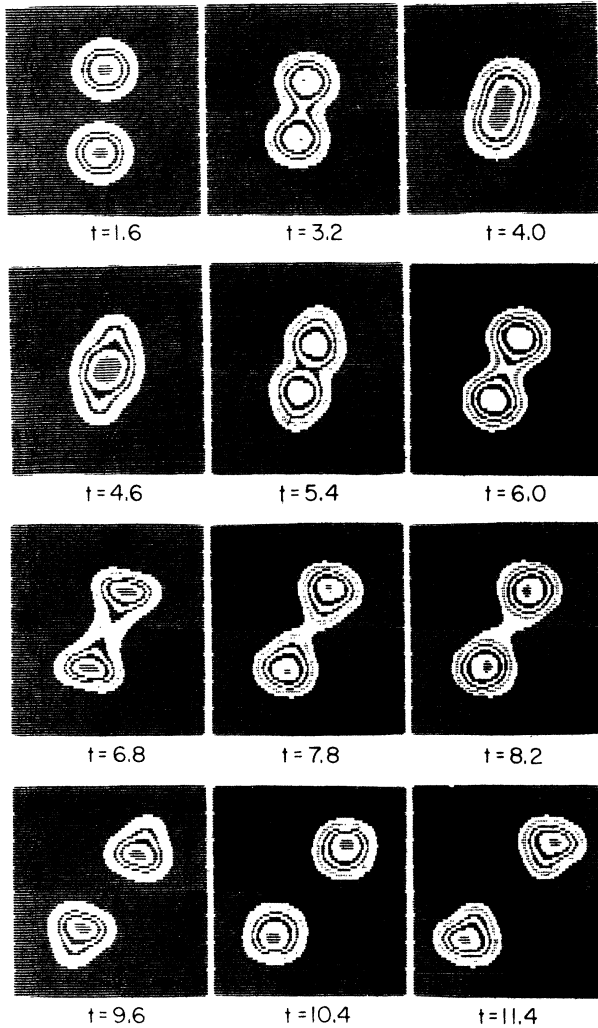


FIG. 3. Contour lines of the density integrated over the coordinate normal to the scattering plane for an $^{16}\text{O} + ^{16}\text{O}$ collision at $E_{\text{lab}} = 105$ MeV and incident angular momentum $L = 5\hbar$. The times t are given in units of 10^{-22} sec.

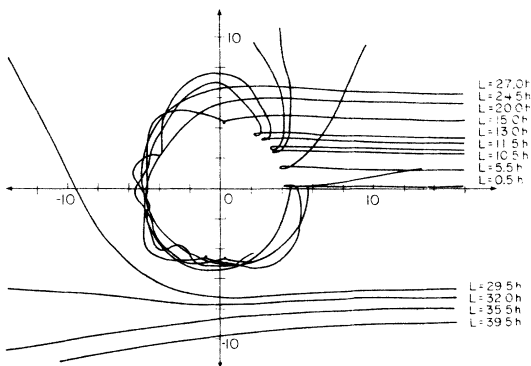


FIG. 4. Trajectories of the vector separation \vec{R} between the centers of mass of the two fragments for incident angular momentum values ranging from 0 to $40\hbar$.

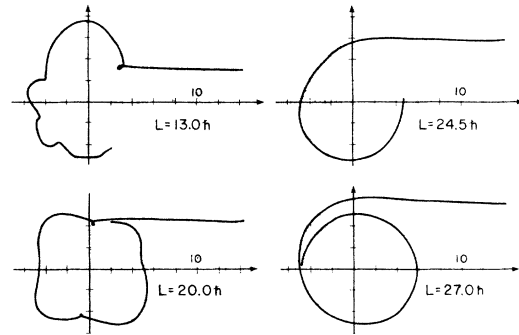


FIG. 5. Examples of different trajectories leading to fusion.

and $25\hbar$) the dominant factors are the nuclear attraction combined with dissipation. These lead to a smooth orbiting trajectory. For lower impact parameters ($L = 13$ and $20\hbar$) the trajectory is more complex. After an initial attraction the two nuclei reach a configuration where the collective potential leads to a repulsion. As the nuclei begin to move apart under the influence of this repulsion, they are unable to separate because of the large amount of energy that has been dissipated.

The third group of trajectories ($L < 13\hbar$) does not lead to fusion. We therefore do not find the expected result that fusion, if it occurs, does so at zero impact parameter. The existence of the low L window for which fusion does not occur is energy-dependent.¹⁹ Indeed, we show in Fig. 6 an example of a trajectory at much lower energy ($E_{\text{lab}} = 32$ MeV) for which a head-on collision does lead to fusion. This had already been noted in Ref. 12 for the $^{40}\text{Ca} + ^{40}\text{Ca}$ system.

In Fig. 7 we display a collision at $E_{\text{lab}} = 192$ MeV and a large impact parameter, 6 fm ($L = 42\hbar$). This figure complements Fig. 2 which showed a fusion process for a small value of the impact pa-

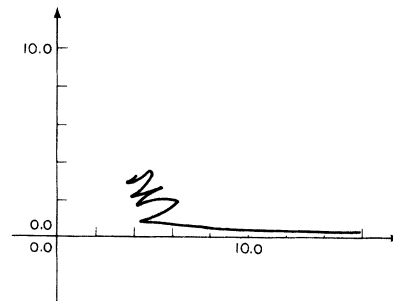


FIG. 6. Trajectory for a nearly head-on collision ($L = 0.5\hbar$) at low energy ($E_{\text{lab}} = 32$ MeV) which leads to fusion.

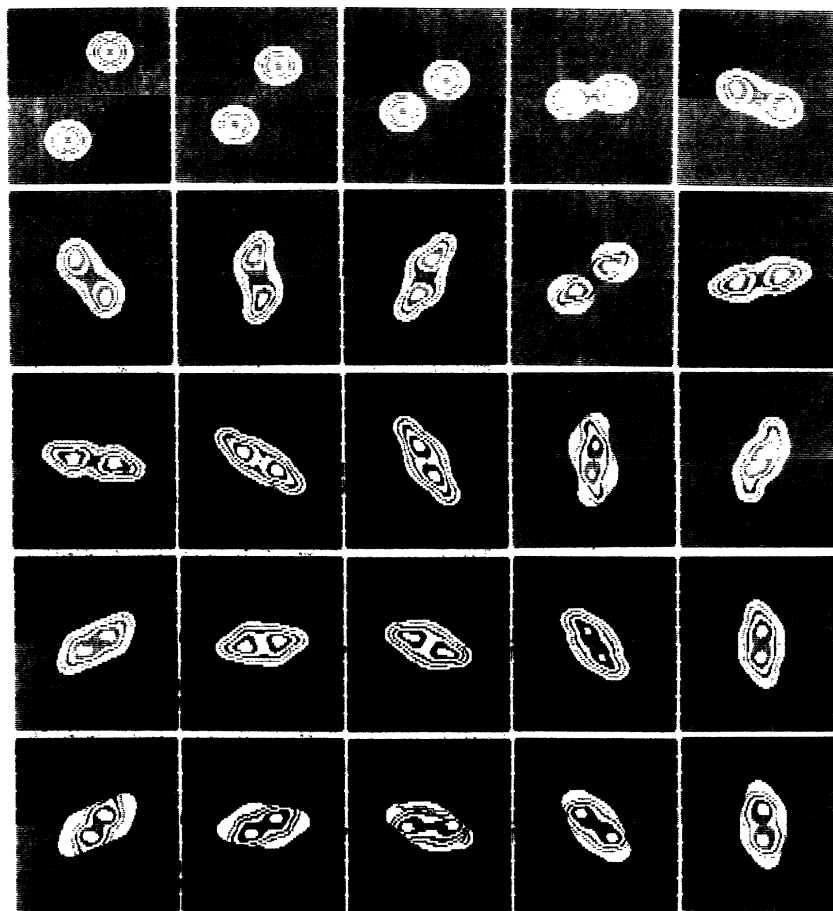


FIG. 7. Contour lines of the density integrated over the coordinate normal to the scattering plane for an $^{16}\text{O} + ^{16}\text{O}$ collision at $E_{\text{lab}} = 192$ MeV and incident angular momentum $L = 42\hbar$. The time interval between two pictures is 10^{-22} sec.

parameter. Nonaxial effects are very important. A comparison of the shapes at $t = 7 \times 10^{-22}$ and 15×10^{-22} sec shows two extreme stages of a wiggling mode. Note how the shape becomes more compact (i.e., more fused) during the collision. A more detailed study of the fusion regime may be found in Ref. 19.

In Fig. 8 we give the deflection angle and the total kinetic energy loss as functions of the angular momentum. For small impact parameters ($L < 13\hbar$) the kinetic energy loss is constant at about 35 MeV, to be compared with the 52.5 MeV available initially in the center-of-mass frame. Because of the total c.m. motion these trajectories would result in fragments moving forward in the laboratory frame. According to our calculations, one would expect heavy fragments moving with kinetic energy ranging between 5 and 65 MeV in a forward cone of about 35° . (Recall that the beam energy is 105 MeV.) Since the fragments are strongly excited the mass distribution would certainly not be centered around

$A = 16$ due to deexcitation via nucleon or α -particle emission. When the fragments emerge, they have nearly the same angular momentum with which they enter. This is in spite of the fact that at times during the collision the total angular momentum is almost entirely absorbed by the internal angular momentum of the fragments.

There is a difference between our results and those of Ref. 16, since we do get fusion. Because the energy used for the $^{16}\text{O} + ^{16}\text{O}$ collisions in Ref. 16 is slightly higher than the one we use (8 instead of 6.6 MeV per nucleon in the lab) we have made one calculation with the energy of Ref. 16 and with an angular momentum $L = 30\hbar$. Consistent with our previous results we find fusion. The trajectory was followed up to a deflection of $-3\pi/2$ without any indication of separation, in contrast to the finite deflection angle $-\pi/3$ found in Ref. 16 (Fig. 7). The difference comes from our inclusion of a Yukawa interaction not present in their calculation. Our interaction provides a

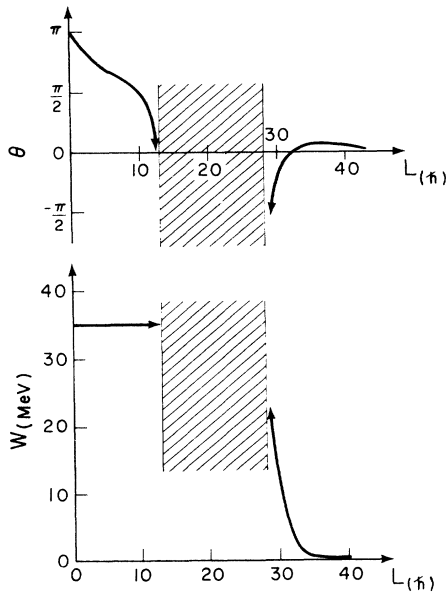


FIG. 8. Deflection angle and kinetic energy loss as functions of incident angular momentum at $E_{lab} = 105$ MeV. The shaded area corresponds to the fusion window.

better reproduction of the surfaces of the nuclei, a feature which is certainly needed to describe correctly heavy-ion collisions, as demonstrated in Ref. 19. However, the apparent sensitivity to the interaction indicated by their results leads us to hope that TDHF calculations combined with appropriate experiments will increase our knowledge of the effective interaction.

VI. DISCUSSION

The most striking feature of our results is the absence of fusion for small values of the incident angular momentum. We find that for any angular momentum from 13 to $27\hbar$ the nuclei "fuse" in the sense that they remain either in close contact for times longer than 3×10^{-21} sec or that the deflection angle exceeds -180° . If we interpret this range of impact parameters classically we obtain a fusion cross section of about 0.8 b.

All trajectories with $L \leq 20\hbar$ exhibit a loop at the point of closest approach, as can be seen in Figs. 4 and 5. At this point, the relative orbital angular momentum of the fragments becomes negative, changing sign from its value at $t=0$. This phenomena has its origin in the single-particle degrees of freedom treated explicitly in a TDHF calculation. Similar behavior, which is due to the motion of the single-particle wave functions in the time-dependent mean field, has been observed in both one-⁹ and two-dimensional¹² cal-

culations; we shall sketch the same reasoning here to explain our three-dimensional results. When the two nuclei begin to interact, the barrier between their separate mean-field potentials disappears and all wave functions begin to move in one large common well. The velocities of the orbitals from one nucleus as they traverse the other nucleus differ according to their internal kinetic energy. Thus, in the $^{16}\text{O} + ^{16}\text{O}$ system, some $1p$ orbitals move faster and reflect first from the opposite wall of the potential. Their resulting backward motion cancels the still forward motion of the remainder of the orbitals. As a result, the net orbital angular velocity of the fragment c.m.'s can become negative. This example of the exchange of angular momentum between single-particle and collective degrees of freedom is the essence of the one-body dissipation process. However, in this relatively small system, the non-statistical dynamics of a few orbitals soon restores much of the angular momentum to the c.m. motion. In fact, there is hardly any angular momentum loss in the low impact-parameter events. In heavier systems, the greater diversity of single-particle motions will affect the collective variables in a much smoother manner,¹⁹ so that the notion of a macroscopic dissipation coefficient may become applicable. One can also note that the significant differences between the different fusion trajectories $13\hbar \leq L \leq 27\hbar$ (Fig. 5) would be difficult to reproduce by a model taking into account only the motion of the c.m.'s.

We have shown that it is unlikely that one could explain *all* our results by a potential and a viscosity coefficient. However, this is still possible within a *limited* range of angular momenta. We demonstrate this for the low values of the angular momentum which lead to inelastic scattering.

For values of L between 0 and $20\hbar$, the point of closest approach corresponds to an almost constant value of the distance between the c.m.'s, 4.1 fm (see Fig. 4). This gives us the location R_B of the internal repulsive part of the heavy-ion nuclear potential (Fig. 9). (Effective mass effects are neglected, as it can generally be done in a one-dimensional problem by a proper redefinition of the potential. The mass is therefore the reduced mass $\mu = 8$ m.) This internal barrier is of dynamical origin and probably comes from the inability of the fragments to significantly change their shell structure during the collision. Static constrained HF calculations performed for the same system,²⁷ which can be thought of as describing the potential for an infinitely slow collision, do not give a potential with an internal barrier. There, the system of 32 nucleons adjusts itself to the best possible shell structure for a

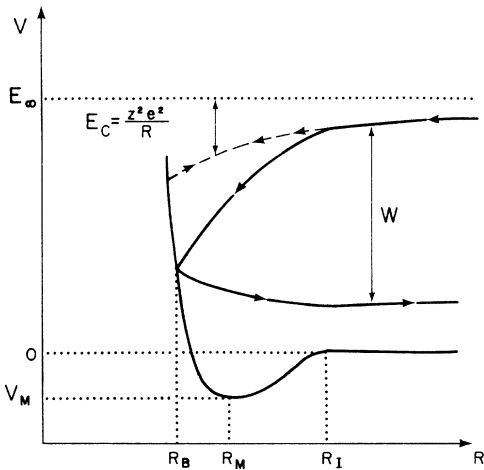


FIG. 9. Schematization of the nuclear part of a heavy-ion potential. E_∞ is the kinetic energy for infinitely separated fragments. The dashed line is a trajectory in the absence of dissipation. It is shifted from E_∞ by the point Coulomb energy E_C . The solid line is a trajectory with dissipation and W stands for the energy loss.

given separation of the c.m.'s. For small separations, the ^{32}S configuration is energetically the most stable. Figure 10 shows the behavior of the single-particle (s.p.) energies as a function of time for a nearly head-on collision ($L = 0.5\hbar$, $E_{1ab} = 105$ MeV). (We define the s.p. energies as the diagonal elements of the matrix $\epsilon_{ij} = \int d\vec{r} \psi_i^* \hat{h} \psi_j$. This is not an unambiguous definition since the ψ_i 's are defined only up to a unitary transformation. Another possibility would be to choose as s.p. energies the eigenvalues of the $\{\epsilon_{ij}\}$ matrix. This choice would probably not change the qualitative aspect of our argument.) Initially, this single-particle spectrum exhibits the degeneracy characteristic of two ^{16}O nuclei. (Recall that our

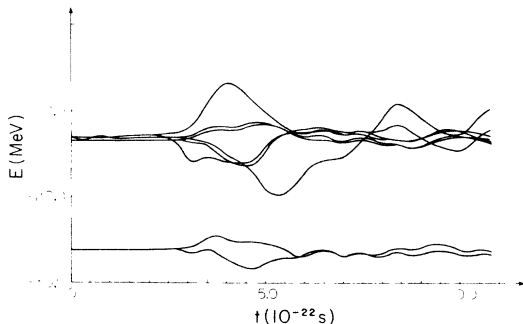


FIG. 10. Time-dependent single-particle energy spectrum (see text) for a nearly head-on collision ($L = 0.5\hbar$, $E_{1ab} = 105$ MeV).

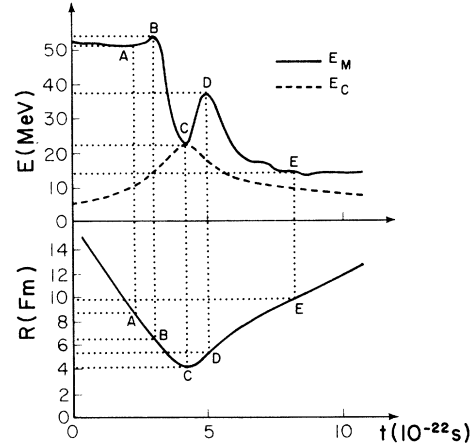


FIG. 11. Upper part: the point Coulomb energy E_C and the mechanical energy E_M (see text) as functions of time for a nearly head-on collision ($L = 0.5\hbar$, $E_{1ab} = 105$ MeV). Lower part: the corresponding time evolution of the fragment separation coordinate.

calculation does not include a spin-orbit force.) The degeneracy is lifted during the collision, although the shell structure is remarkably well preserved and the spectrum never comes close to that of ^{32}S . Since the distance of closest approach R_B is almost independent of the angular momentum, the potential at that point must be very steep. Indeed, although the classical centrifugal energy $\hbar^2 L^2 / 2\mu R_B^2$ changes by about 60 MeV for L varying between 0 and $20\hbar$, its effect on R_B is very small. This stiffness of the potential is confirmed by the fact that R_B is independent of the incident energy, as can be seen in Fig. 6 ($E_{1ab} = 32$ MeV).

To pursue the analysis, the velocities of the c.m.'s must be considered. We do this in Fig. 11, which again corresponds to the $L = 0.5\hbar$, $E_{1ab} = 105$ MeV collision. The energy E_C in the upper part of the figure is the point Coulomb energy $Z^2 e^2 / R$. We have also plotted the quantity E_M which is larger than E_C by the total kinetic energy of the relative motion of the c.m.'s. The evolution of E_M can be understood in terms of a motion with dissipation in a collective potential well such as that shown in Fig. 9. Between the initial time and point A, E_M is constant. (The small decrease of ~ 1 MeV is due to the numerical inaccuracies discussed in Appendix A. It is a measure of the precision of our calculations.) The point A corresponds to the beginning of the nuclear interaction; neglecting internal degrees of freedom makes E_M the total energy before the nuclear interaction begins. We have, therefore, an estimate of the distance at which nuclear effects become important: $R_I = 8.5$ fm. Between A and B, E_M increases, correspond-

ing to motion in the descending part of the potential. However, the increase of E_M is less than the depth of the potential V_M because of dissipative effects. For the same reason the distance between the c.m.'s at point B is larger than R_M (Fig. 9). Between B and C the potential rises, therefore E_M decreases until it equals the Coulomb energy E_C . The distance between the c.m.'s at point C gives the radius of the internal core R_B . The points D and E are the analogs of B and A on the outgoing part of the trajectory. This time, because of the dissipative effects, the distance between the c.m.'s at point D gives a lower limit for the value of R_M . The distance at the last point of interaction E is larger than the distance at point A reflecting both fragment elongation and an overall increase in the size of the fragments after the collision. For example, the root-mean-square radius of the fragments increases by about 0.3 fm as a consequence of the transfer of energy to the internal degrees of freedom of the fragments. If there were no dissipation of the radial motion, all the curves shown in Fig. 11 would be symmetric with respect to the vertical line going through point C . Analyzing the extrema of the energy curve $E_M(t)$ and the distance curve $R(t)$ with the above interpretation gives a minimum in the nuclear potential between -14 and -24 MeV at a distance between 5.5 and 6.5 fm. The upper boundary for the depth of potential (24 MeV) is obtained with the assumption that the dissipation of E_M occurs only when the two nuclei move toward each other (faster velocities). If one were to assume that the same amount of energy is lost during the ingoing and outgoing phases of motion, the lower value (14 MeV) would be obtained.

The energy loss for $L = 0.5\hbar$, $E_{1ab} = 105$ MeV is about 35 MeV. Within the precision of our calculation (1 MeV) this number is constant for L varying between 0 and $11\hbar$ (Fig. 8). This indicates that for these values of the angular momentum it is not necessary to introduce a tangential friction. Using a simple model, neglecting potential effects in first approximation and assuming a viscosity proportional to the relative radial velocity of the c.m.'s acting for a distance equal to $2(R_T - R_B)$, we find that a radial viscosity coefficient of 2×10^{-22} MeV fm⁻² sec explains our 35 MeV energy loss. Within the same crude model this viscosity leads to a value of 0.9 MeV per nucleon in the c.m. ($E_{1ab} = 58$ MeV) for the threshold of *no fusion* at $L = 0\hbar$, in good agreement with the results of Ref. 19. Although we are not in a position to discuss the energy dependence of the collective potential, we note that this dependence will arise naturally in similar analyses of TDHF calculations at other energies.

VII. CONCLUSION

The most interesting phenomenon we have observed in our calculation is a region of fusion which yields a fusion cross section consistent with experiment.²⁸ This is in contrast to previous calculations in two dimensions¹¹⁻¹³ which showed no fusion for high-energy collisions. Therefore, nonaxiality is important in the dissipative process that leads to fusion.

It is also important to note the lack of fusion for small angular momentum at high bombarding energy. For these small values of the angular momentum we calculate the scattering angle and energy loss of the outgoing fragments. These predictions are amenable to experimental verification. We also find that the absence of fusion for head-on collisions disappears at sufficiently low bombarding energies. However, our calculations contain several technical restrictions (e.g., spin, isospin, and two spatial symmetries) which may affect the specific numerical values presented in this paper.

A comparison with other 3D calculations¹⁶ indicates a dependence of the results on the effective interaction. This dependence is confirmed by the detailed study of the fusion excitation function contained in Ref. 19. For this reason the TDHF method appears as a promising tool for extracting additional knowledge of the nucleon-nucleon effective interaction from the experimental data on heavy-ion scattering.

ACKNOWLEDGMENTS

We have benefited from numerous discussions with our colleagues and in particular wish to thank R. Cusson, N. K. Glendenning, J. Griffin, D. Hendrie, D. Scott, and W. Swiatecki. Special thanks are due D. Vautherin for many comments and a critical reading of the manuscript. Lastly, we would like to acknowledge A. K. Kerman for his unstinting stimulation. One of us (H. F.) would also like to thank N. K. Glendenning for the hospitality of the Nuclear Theory Group at the Lawrence Berkeley Laboratory. This work was done with the support of the U. S. Energy Research and Development Administration and the National Science Foundation.

APPENDIX A: DISCRETE REPRESENTATION OF THE TDHF EQUATIONS

We solve the TDHF equations in coordinate space using methods similar to those of Refs. 9 and 12. In our three-dimensional calculations, the single-particle wave functions are described by their values on a uniformly spaced Cartesian

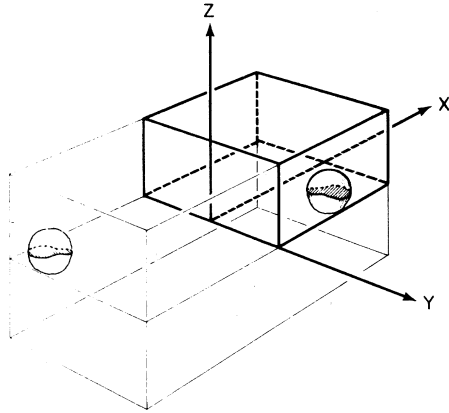


FIG. 12. The thick lines indicate the box in which the calculations are actually performed and the thin lines show the complete box deduced by means of the two spatial symmetries imposed. The gray surface indicates a possible equidensity contour surface with the same convention.

mesh contained within a rectangular box. Vanishing boundary conditions are imposed outside of this box. The choices of box dimensions and mesh spacing are influenced by two competing considerations. On one hand, computing speed and storage considerations favor a small box and large mesh spacing to reduce the number of variables describing the system. On the other hand, the box must be large enough to contain the TDHF solution without the system “hitting the walls” and the mesh spacing must be small enough to give an accurate representation of the TDHF energy functional. Our method therefore employs a relatively large mesh spacing (1 fm in all three directions) yet uses high-order discretizations of the kinetic energy and Yukawa potentials. The box size has been varied according to the collision being calculated. We choose the center of the box to be the time-independent c.m. of the whole system and orient the reaction plane normal to one edge (z axis). Typical box dimensions are 30 fm \times 28 fm \times 16 fm in the x , y , and z directions, respec-

tively. The spatial symmetries we impose on the determinant (cf. Sec. III) restrict the actual numerical work to one-quarter of the box volume. How these symmetries are implemented in our code is described in Fig. 12. As discussed in Appendix C, the nonconservation of energy associated with the boundary conditions of the Yukawa potential provides a stringent check against spurious effects of the mesh boundaries.

A discrete representation of the TDHF Hamiltonian can be obtained by the variation of a discrete approximation to the energy functional with respect to the values of the single-particle wave functions at the mesh points. This procedure preserves the variational aspects of the discrete TDHF equations. It has been discussed in detail for cylindrical coordinate systems in Ref. 12 and can be extended directly to three Cartesian dimensions. We therefore discuss only those new problems presented by the three-dimensional calculations.

Experience has shown that the zero-range (t_0 and t_3) terms of the energy functional [Eq. (6)] are accurately discretized on our large mesh spacing by a trapezoidal approximation to the integrals (cf. Table II). Similarly, an adequate accuracy is easily achieved for the Coulomb energy (cf. Appendix C). However, the accuracy of the discrete approximations to the kinetic energy and short-range Yukawa potential is very sensitive to the mesh spacing and techniques used. We treat the kinetic energy below and discuss the Yukawa potential in Appendix C.

The total kinetic energy is the sum of the kinetic energies for each of the single-particle wave functions in each of the three spatial directions. It is therefore sufficient to consider a single wave function in one dimension. The fundamental quantity we are interested in approximating is then

$$T_i \equiv \frac{1}{2} \int_{x_i - \Delta x}^{x_i + \Delta x} dx \left| \frac{\partial \psi}{\partial x} \right|^2, \quad (\text{A1})$$

where x_i is the coordinate at the i th mesh point,

TABLE II. Contributions to the total energy of two ^{16}O nuclei as described in the text (values in MeV).

	Kinetic energy	Contribution of $t_0 \delta(\vec{r}_1 - \vec{r}_2)$	Contribution of $\frac{1}{6} t_3 \delta(r_1 - r_2)$	Yukawa energy	Coulomb energy
Discrete energy functional	457.560	-423.785	230.088	-458.594	36.752
Analytic value	460.504	-423.784	230.100	-458.393	36.489

Δx is the mesh spacing, and $\psi(x)$ is the wave function. A Taylor expansion of T_i in Δx leads to

$$T_i = \Delta x \left| \psi_i^{(1)} \right|^2 + \frac{1}{3} (\Delta x)^3 \operatorname{Re}(\psi_i^{(1)*} \psi_i^{(3)} + \left| \psi_i^{(2)} \right|^2) + \frac{(\Delta x)^5}{60} \operatorname{Re}(\psi_i^{(1)*} \psi_i^{(5)} + 2\psi_i^{(2)*} \psi_i^{(4)} + 3 \left| \psi_i^{(3)} \right|^2) + \mathcal{O}((\Delta x)^7). \quad (\text{A2})$$

The notation $\psi_i^{(n)}$ is used here for the n th derivative of ψ at x_i .

The lowest order difference approximation to $\left| \psi_i^{(1)} \right|^2$ results in the three-point approximation to the kinetic energy²⁹

$$T_i^{(3)} = \frac{1}{2\Delta x} \left(\left| \psi_{i+1} - \psi_i \right|^2 + \left| \psi_i - \psi_{i-1} \right|^2 \right). \quad (\text{A3})$$

The variation of the quantity $T_i^{(3)}$ with respect to ψ_i^* leads directly to the three-point approximation for $\psi_i^{(2)}$ used in Ref. 12. A simple analysis of $T_i^{(3)}$ gives

$$T_i^{(3)} = \Delta x \left| \psi_i^{(1)} \right|^2 + \frac{1}{3} (\Delta x)^3 \operatorname{Re}(\psi_i^{(1)*} \psi_i^{(3)} + \frac{3}{4} \left| \psi_i^{(2)} \right|^2) + \mathcal{O}((\Delta x)^5) \quad (\text{A4})$$

so that the error term in $T_i^{(3)}$ is $\mathcal{O}((\Delta x)^3)$.

The next order approximation to the kinetic energy is obtained by using an approximation of the form

$$T_i^{(5)} = \frac{1}{2(\Delta x)} \left(\left| b_- \psi_{i-1} + b_0 \psi_i + b_+ \psi_{i+1} \right|^2 + \left| b_+ \psi_{i-1} + b_0 \psi_i + b_- \psi_{i+1} \right|^2 \right), \quad (\text{A5})$$

where the coefficients $b_{0,\pm}$ are chosen so that $T_i^{(5)}$ approximates T_i to $\mathcal{O}((\Delta x)^5)$:

$$b_0 = \frac{2}{\sqrt{3}}, \quad (\text{A6})$$

$$b_{\pm} = -\frac{1}{\sqrt{3}} \pm \frac{1}{2}.$$

The variation of $T_i^{(5)}$ leads to a five-point approximation to $\psi_i^{(2)}$.²⁹ The error term is $\mathcal{O}((\Delta x)^5)$:

$$T_i - T_i^{(5)} = \frac{(\Delta x)^5}{90} \operatorname{Re}(\psi_i^{(2)*} \psi_i^{(4)} + 2 \left| \psi_i^{(3)} \right|^2). \quad (\text{A7})$$

[Our choice (A6) is one member of a one-parameter family of complex solutions $b_0 = 2/\sqrt{3}$, $b_{\pm} = -1/\sqrt{3} \pm \frac{1}{2} e^{i\alpha}$, $0 \leq \alpha \leq \pi$. Equation (A7) holds for any value of α .]

The use of the five-point approximation for the kinetic energy operator complicates the time evolution of the TDHF equations. For example, in one dimension the HF Hamiltonian is then represented by a pentadiagonal matrix, rather than a tridiagonal one. However, in view of the 1-fm mesh spacing we are forced to use, the extra effort is justified, as can be seen by a simple ex-

TABLE III. The kinetic energy of the ground state of a one-dimensional oscillator potential ($m\omega/\hbar = 0.275 \text{ fm}^{-2}$) calculated with the three- and five-point formulas. Δx is the mesh spacing.

Δx (fm)	Kinetic energy (MeV)	3-point formula	5-point formula
	Analytic value		2.8512
0.5		2.8269	2.8507
0.75		2.7968	2.8485
1.0		2.7554	2.8430
1.25		2.7034	2.8320

ample. We have calculated the kinetic energy of the lowest state in a one-dimensional oscillator potential with oscillator parameter $m\omega/\hbar = 0.275 \text{ fm}^{-2}$, a typical number for nuclear problems. The results of the three- and five-point formulas with various mesh sizes are shown in Table III. The superiority of the five-point method is evident. In fact, with a mesh spacing of 1 fm, this method is more accurate than the three-point method with $\Delta x = 0.5 \text{ fm}$.

The translational invariance of the TDHF equations is also affected by our discretization procedure. We apply the gauge transformation $e^{i\vec{k}\cdot\vec{r}}$ to the orbitals of the static HF solution in order to generate the initial state of a nucleus moving with velocity $\vec{v} = \hbar\vec{k}/m$. Because we use a Galilean-invariant two-body interaction, the HF potential is unaffected by this boost and the single-particle kinetic energy of each orbital increases by the translational kinetic energy $E_T = \frac{1}{2} m v^2$. Although these properties are true for the TDHF equations, they need not hold for their discrete approximations. In order to test this aspect of our discretization, we have applied various boosts to the ground-state oscillator wave function used to construct Table III. Our results are shown in Fig. 13 where we display the fractional difference between the calculated kinetic energies of the boosted and stationary states. For the calculations presented in this paper ($E_T \leq 2 \text{ MeV}$), the general level of accuracy should be 1 to 2% and for $E_T < 25 \text{ MeV}$, the five-point formula with $\Delta x = 1 \text{ fm}$ is more accurate than the three-point formula with $\Delta x = 0.5 \text{ fm}$. Despite this encouraging fact, some caution is necessary in applying these results to our actual calculations. Figure 13 refers to the lowest state of an oscillator well. However, our nuclei also contain p -shell orbitals. The difference formulas are less accurate for these higher lying states, so that for ^{16}O the translational kinetic energy of the boosted nucleus is in error by as much as 5%. The different errors

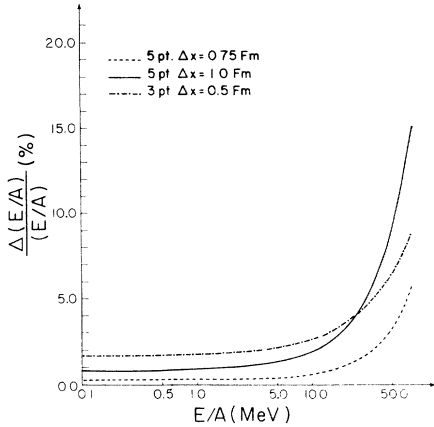


FIG. 13. Relative error in the kinetic energy of the lowest state of an oscillator. The results are shown for the five-point and three-point formulas of the kinetic energy and different mesh sizes. The oscillator parameter is $m\omega/\hbar = 0.275 \text{ fm}^{-2}$.

in the different wave functions also lead in a different way to the breaking of translational invariance for the discrete equation. Because of differencing errors, the transformation $e^{i\vec{k}\cdot\vec{r}}$ sets each orbital in motion with a slightly different velocity. Since the HF mean field binds all orbitals together, some energy is gradually transferred from translation into internal excitation. In $^{16}\text{O} + ^{16}\text{O}$, this phenomenon leads to at most a 7% loss in translational kinetic energy in our calculation over a time of 1.5×10^{-21} sec.

We close this Appendix with an overall assessment of the accuracy of our discretization of the energy functional. We consider two ^{16}O nuclei built from oscillator wave functions ($m\omega/\hbar = 0.275 \text{ fm}^{-2}$) and positioned 16 fm apart. They are boosted toward each other with a translational kinetic energy per nucleon of $E_T = 1.74 \text{ MeV}$. In Table II we show the calculated ($\Delta x = \Delta y = \Delta z = 1 \text{ fm}$, five-point formula) and analytic contributions to the energy functional. The Coulomb and Yukawa energies have been calculated as described in Appendix C; the overall accuracy is quite acceptable, with the most serious discrepancy being some 3 MeV out of 460 MeV in the kinetic energy.

APPENDIX B: SOLUTION OF THE TDHF EQUATIONS WITH A FINITE TIME STEP

Conservation of the total energy

Although the discussion contained in this appendix is valid for any two-body interaction, we discuss here only the case of a zero-range interaction which depends linearly on the density. We therefore deal only with the density and the kinetic

energy density [Eqs. (4) and (5)]. However, it is straightforward to show that our arguments can be extended to the full one-body density operator, i.e., to any two-body interaction. We shall also neglect the spin and isospin degrees of freedom which are irrelevant to the argument.

If $\{\psi_j^{(n)}\}$ ($1 \leq j \leq A$) is a set of single-particle wave functions at time step n , the HF energy at that time step for a two-body interaction

$$v_2 \equiv t_0 \delta(\vec{r}_1 - \vec{r}_2) + \frac{1}{6} t_3 \rho \left[\frac{1}{2} (\vec{r}_1 + \vec{r}_2) \right] \delta(\vec{r}_1 - \vec{r}_2)$$

is

$$E^{(n)} = \int d\vec{r} \left(\frac{\hbar^2}{2m} \tau^{(n)}(\vec{r}) + \frac{3}{8} t_0 \rho^{(n)}(\vec{r})^2 + \frac{1}{16} t_3 \rho^{(n)}(\vec{r})^3 \right), \quad (\text{B1})$$

where $\rho^{(n)}(\vec{r})$ and $\tau^{(n)}(\vec{r})$ are, respectively, the density and kinetic energy density at time step n .

If $\{\psi_j^{(n+1)}\}$ is the set of single-particle wave functions at time step $(n+1)$, we define the quantity $\delta\rho$ as

$$\delta\rho \equiv \rho^{(n+1)} - \rho^{(n)} = \sum_{j=1}^A |\psi_j^{(n+1)}|^2 - |\psi_j^{(n)}|^2. \quad (\text{B2})$$

In the same way we have

$$\delta\tau \equiv \tau^{(n+1)} - \tau^{(n)}. \quad (\text{B3})$$

Some algebraic manipulations then show that

$$\rho^{(n+1)2} = \rho^{(n)2} + \delta\rho(\rho^{(n+1)} + \rho^{(n)}), \quad (\text{B4})$$

$$\rho^{(n+1)3} = \rho^{(n)3} + \delta\rho(\rho^{(n+1)2} + \rho^{(n)}\rho^{(n+1)} + \rho^{(n)2}). \quad (\text{B5})$$

These equations are exact and do not represent a truncated expansion of $\rho^{(n+1)2}$ and $\rho^{(n+1)3}$. With Eqs. (B4) and (B5) the energy at time $n+1$, $E^{(n+1)}$ can therefore be written as

$$E^{(n+1)} = E^{(n)} + \sum_{j=1}^A \int d\vec{r} \left(\psi_j^{(n+1)*} h^{(n+1/2)} \psi_j^{(n+1)} - \psi_j^{(n)*} h^{(n+1/2)} \psi_j^{(n)} \right), \quad (\text{B6})$$

where the Hamiltonian $h^{(n+1/2)}$ is defined as

$$h^{(n+1/2)} = -\frac{\hbar^2}{2m} \nabla^2 + \frac{3}{8} t_0 (\rho^{(n)} + \rho^{(n+1)}) + \frac{1}{16} t_3 (\rho^{(n)2} + \rho^{(n)}\rho^{(n+1)} + \rho^{(n+1)2}).$$

In order to conserve the energy exactly, the $\psi_j^{(n+1)}$'s must be constructed so as to cancel the second term of the right-hand side of (B6). Then choosing

$$\psi_j^{(n+1)} = U \psi_j^{(n)}, \quad (\text{B7})$$

where U is any unitary operator which commutes with $h^{(n+1/2)}$ will lead to an exact cancellation of $(E^{(n+1)} - E^{(n)})$. Since we want to use a numerical

scheme for approximating the continuous TDHF equations

$$i\hbar \frac{\partial \psi_j}{\partial t} = h \psi_j, \quad (\text{B8})$$

$$h = -\frac{\hbar^2}{2m} \nabla^2 + \frac{3}{4} t_0 \rho + \frac{3}{16} t_3 \rho^2 \quad (\text{B9})$$

we can use the unitary operator

$$U_E = \exp\left(-i \frac{\Delta t}{\hbar} h^{(n+1/2)}\right), \quad (\text{B10})$$

or any unitary approximation to the exponential, such as the Crank-Nicholson (CN) operator:

$$U_{\text{CN}} = \frac{1 - (i\Delta t/2\hbar)h^{(n+1/2)}}{1 + (i\Delta t/2\hbar)h^{(n+1/2)}}. \quad (\text{B11})$$

For the calculations presented in this paper we have expanded the exponential operator U_E in a power series to $\mathcal{O}(\Delta t^5)$. Indeed, as the discretized operator $h^{(n+1/2)}$ amounts to a 3000×3000 dense matrix for a typical mesh size, it would be difficult to use the exact exponential operator. In fact with a time step of 4×10^{-24} sec, five terms in the exponential suffice to conserve the wave function norm to one part in 10^6 and the total energy of the system to better than 0.5% (~ 1 MeV) over periods longer than 1.5×10^{-21} sec, a typical collision time.

The relation between $h^{(n+1/2)}$, and the Hamiltonians $h^{(n)}$ and $h^{(n+1)}$ defined by

$$h^{(n)} = -\frac{\hbar^2}{2m} \nabla^2 + \frac{3}{4} t_0 \rho^{(n)} + \frac{3}{16} t_3 \rho^{(n)2} \quad (\text{B12})$$

is

$$h^{(n+1/2)} = \frac{1}{2} (h^{(n)} + h^{(n+1)}) - \frac{1}{32} t_3 (\rho^{(n+1)} - \rho^{(n)})^2. \quad (\text{B13})$$

Thus the construction of $h^{(n+1/2)}$ requires the knowledge of the $\{\psi_j^{(n+1)}\}$, which are not known ahead of time. In practice we use the following procedure. From the Hamiltonians $h^{(n)}$, $h^{(n-1)}$, and $h^{(n-2)}$, we construct with Lagrange extrapolation a first guess of $h^{(n+1/2)}$. We then compute a first estimate of $\{\psi_j^{(n+1)}\}$ with U_E . We can then obtain $h^{(n+1)}$ and a better approximation of $h^{(n+1/2)}$ using the formulas (B12) and (B13). Finally we compute the $\psi_j^{(n+1)}$'s with U_E . It can be shown that further iterations of this procedure combined with an exact handling of the operators U_E or U_{CN} would lead to a convergence toward the exact solution $h^{(n+1/2)}$, and therefore an exact conservation of the energy. The method used in this paper has therefore the advantage of being easily controlled for any value of the time step by increasing either the number of terms in the expansion of U_E or the number of iterations in the calculation of $h^{(n+1/2)}$. In practice

we found that to reach a precision of 1 MeV in the conservation of the energy, one iteration in the calculation of $h^{(n+1/2)}$ sufficed ($\Delta t = 4 \times 10^{-24}$ sec). In addition, the precision required (i.e., the number of terms in the expansion of U_E) to obtain the first estimate of $\{\psi_j^{(n+1)}\}$ is less than the precision needed for the final set of $\psi_j^{(n+1)}$'s. In practice, the first two terms in the exponential operator are sufficient.

Comparison with the exact solution

We will restrict our discussion to the case of the exponential operator U_E [formula (B10)] and mention at the end of the Appendix the results obtained with the CN method and two approximations to the CN method: the alternating direction (AD) and the local one-dimensional method (LOD).³⁰

With the exponential operator the wave functions at time Δt , $\{\psi_j^{(1)}\}$, are obtained from the wave functions at time zero, $\{\psi_j^{(0)}\}$, as

$$\psi_j^{(1)} = \exp\left(-\frac{i}{\hbar} \Delta t h^{(1/2)}\right) \psi_j^{(0)}, \quad (\text{B14})$$

where the operator $h^{(1/2)}$ is constructed according to formula (B13). It will make the discussion shorter to restrict ourselves to the case where only two-body interactions are included in the Hamiltonian \hat{H} . The reader may convince himself that the results presented hereafter remain true when the zero-range density-dependent interaction is also present. For a Hamiltonian with only two-body interactions the operator $h^{(1/2)}$ may be written as

$$h^{(1/2)} = \frac{1}{2} (h^{(0)} + h^{(1)}). \quad (\text{B15})$$

For our purposes, it is convenient to emphasize the functional dependence of the HF Hamiltonian $h^{(0)}$ and $h^{(1)}$ on the wave functions ψ_j and their conjugates ψ_j^* by writing

$$h^{(0)} \equiv h(\{\psi_j^{(0)}, \psi_j^{(0)*}\}), \quad (\text{B16})$$

$$h^{(1)} \equiv h(\{\psi_j^{(1)}, \psi_j^{(1)*}\}), \quad 1 \leq j \leq A.$$

In this paper the functional dependence comes only through the density ρ [Eq. (4)] but with other interactions, such as the full Skyrme force,⁸ the kinetic energy and the current would also appear in the expression of h . In order to determine the precision of the exponential scheme, we shall study the derivatives

$$\left. \frac{\partial^n \psi_j^{(1)}}{\partial (\Delta t)^n} \right|_{\Delta t=0} \quad (\text{B17})$$

and compare them with the derivatives of the exact solution $\psi_j(t)$

$$\left. \frac{\partial^n \psi_j}{\partial t^n} \right|_{t=0} \quad (\text{B18})$$

of the TDHF equations

$$\begin{aligned} \frac{\partial \psi_j}{\partial t} &= -\frac{i}{\hbar} h \psi_j, \\ \psi_j(t=0) &\equiv \psi_j^{(0)}. \end{aligned} \quad (\text{B19})$$

The expressions for the first three derivatives of the exact solution at $t=0$ are

$$\left. \frac{\partial \psi_j}{\partial t} \right|_{t=0} = -\frac{i}{\hbar} h^{(0)} \psi_j^{(0)}, \quad (\text{B20a})$$

$$\left. \frac{\partial^2 \psi_j}{\partial t^2} \right|_{t=0} = \left(-\frac{i}{\hbar} h^{(0)} \right)^2 \psi_j^{(0)} - \frac{i}{\hbar} \frac{\partial h^{(0)}}{\partial t} \psi_j^{(0)}, \quad (\text{B20b})$$

$$\begin{aligned} \left. \frac{\partial^3 \psi_j}{\partial t^3} \right|_{t=0} &= \left(-\frac{i}{\hbar} h^{(0)} \right)^3 \psi_j^{(0)} + \left(-\frac{i}{\hbar} \right)^2 \\ &\times \left(h^{(0)} \frac{\partial h^{(0)}}{\partial t} + 2 \frac{\partial h^{(0)}}{\partial t} h^{(0)} \right) \psi_j^{(0)} \\ &- \frac{i}{\hbar} \frac{\partial^2 h^{(0)}}{\partial t^2} \psi_j^{(0)}. \end{aligned} \quad (\text{B20c})$$

In Eqs. (B20a)–(B20c) the expression $\partial h^{(0)}/\partial t$ should be understood as the one-body operator

$$\frac{\partial h^{(0)}}{\partial t} \equiv \left(\sum_{j=1}^A \frac{\partial h}{\partial \psi_j} \frac{\partial \psi_j}{\partial t} + \frac{\partial h}{\partial \psi_j^*} \frac{\partial \psi_j^*}{\partial t} \right) \Big|_{t=0}. \quad (\text{B21})$$

From the definition (B14) and using (B15), we have

$$\left. \frac{\partial \psi_j^{(1)}}{\partial \Delta t} \right|_{\Delta t=0} = -\frac{i}{\hbar} h^{(0)} \psi_j^{(0)} = \left. \frac{\partial \psi_j}{\partial t} \right|_{t=0} \quad (\text{B22})$$

and

$$\left. \frac{\partial^2 \psi_j^{(1)}}{\partial (\Delta t)^2} \right|_{\Delta t=0} = \left(-\frac{i}{\hbar} h^{(0)} \right)^2 \psi_j^{(0)} - 2 \frac{i}{\hbar} \frac{\partial h^{(1/2)}}{\partial \Delta t} \Big|_{\Delta t=0} \psi_j^{(0)}. \quad (\text{B23})$$

From relation (B15) one has

$$\begin{aligned} \left. \frac{\partial h^{(1/2)}}{\partial \Delta t} \right|_{\Delta t=0} &= \frac{1}{2} \left. \frac{\partial h^{(1)}}{\partial \Delta t} \right|_{\Delta t=0} \\ &= \frac{1}{2} \sum_{j=1}^A \left(\frac{\partial h}{\partial \psi_j} \frac{\partial \psi_j^{(1)}}{\partial \Delta t} + \frac{\partial h}{\partial \psi_j^*} \frac{\partial \psi_j^{(1)*}}{\partial \Delta t} \right) \Big|_{\Delta t=0} \\ &= \frac{1}{2} \sum_{j=1}^A \left(\frac{\partial h}{\partial \psi_j} \frac{\partial \psi_j}{\partial t} + \frac{\partial h}{\partial \psi_j^*} \frac{\partial \psi_j^*}{\partial t} \right) \Big|_{t=0} \\ &= \frac{1}{2} \frac{\partial h^{(0)}}{\partial t}. \end{aligned} \quad (\text{B24})$$

In order to obtain the last equalities in the above formula we have used the result (B22). Finally, combining (B23) and (B24), we get

$$\left. \frac{\partial^2 \psi_j^{(1)}}{\partial (\Delta t)^2} \right|_{\Delta t=0} = \left. \frac{\partial^2 \psi_j}{\partial t^2} \right|_{t=0}. \quad (\text{B25})$$

A similar derivation gives for the third-order derivative

$$\begin{aligned} \left. \frac{\partial^3 \psi_j^{(1)}}{\partial (\Delta t)^3} \right|_{\Delta t=0} &= \left(-\frac{i}{\hbar} h^{(0)} \right)^3 \psi_j^{(0)} \\ &+ 3 \left(-\frac{i}{\hbar} \right)^2 \frac{\partial}{\partial \Delta t} (h^{(1/2)}) \Big|_{\Delta t=0} \psi_j^{(0)} \\ &- 3 \frac{i}{\hbar} \left(\frac{\partial^2 h^{(1/2)}}{\partial (\Delta t)^2} \Big|_{\Delta t=0} \right) \psi_j^{(0)}. \end{aligned} \quad (\text{B26})$$

Using the formulas (B24) and (B26) and a relation similar to (B24) for the second derivative of $h^{(1/2)}$, one obtains

$$\begin{aligned} \left. \frac{\partial^3 \psi_j^{(1)}}{\partial (\Delta t)^3} \right|_{\Delta t=0} - \left. \frac{\partial^3 \psi_j}{\partial t^3} \right|_{t=0} \\ = -\frac{i}{2\hbar} \left[\frac{\partial^2 h^{(0)}}{\partial t^2} + \frac{i}{\hbar} \left(\frac{\partial h^{(0)}}{\partial t} h^{(0)} - h^{(0)} \frac{\partial h^{(0)}}{\partial t} \right) \right] \psi_j^{(0)}. \end{aligned} \quad (\text{B27})$$

From the results of (B22), (B25), and (B27) one sees that the exponential method with the operator defined by (B15) ensures that the numerical solution obtained at time Δt is equal to the exact solution through order $(\Delta t)^2$.

A similar analysis of the CN scheme leads to the same condition but with another value for the difference between the exact and numerical third-order derivatives. The reason for our choice of the exponential operator was therefore not the better theoretical precision achieved, but the analytical properties of the exponential. Indeed, it is difficult to apply the exact operators U_E and U_{CN} . (In fact we tested the CN method with the exact inversion performed by means of the conjugate gradient method presented in Appendix C. However, this proved to be more time consuming for a given accuracy than using the expansion of the exponential.) Instead we use an expansion in powers of Δt for which the always convergent expansion of the exponential is more appropriate than the expansion of $1/(1+x)$ associated with the CN method. [From the above analysis one could be led to believe that an expansion of the exponential up to the order $(\Delta t)^3$ is sufficient. However, one has to use more terms in order to conserve both norm and energy]. Two other methods, the alternating direction method and the local one-dimensional method have been shown to be equivalent to the CN method up to the order $(\Delta t)^3$ (Ref. 30). They therefore achieve the same precision as the method used in this paper, although with a somewhat greater numerical complexity.

It should be noted that the analysis made in this Appendix is restricted to one time step (local error analysis). As far as we know there is no rig-

orous way to estimate the error after a given number of time steps, or better, a given evolution time (global error analysis). In order to estimate the quality of the method used in this paper we have made a calculation of a nuclear collision with time steps differing by a factor 2 ($\Delta t = 2$ and 4×10^{-24} sec) and checked that the results remained identical up to the fifth figure during and at the end of the collision.

APPENDIX C: DETERMINATION OF THE COULOMB AND YUKAWA POTENTIALS

The one-body Yukawa and Coulomb potentials are given by Eqs. (8b) and (8c) as convolutions over the nucleon density (recall $\rho_p = \frac{1}{2}\rho$ because of the isospin symmetry we impose). Since these potentials are evaluated many times during each collision (twice per time step), a direct integration is not possible. We therefore follow the strategy of Ref. 12 and calculate the potentials as the solutions of the discrete Poisson and Helmholtz problems

$$\begin{aligned} \nabla^2 W_C &= -2\pi e^2 \rho, \\ (\nabla^2 - 1/a^2) W_Y &= -4\pi V_0 a \rho. \end{aligned} \quad (C1)$$

Here, W_C , W_Y , and ρ are column vectors whose components are the values of these functions on the mesh points and ∇^2 is a sparse matrix approximation to the three-dimensional Laplacian operator. W_C is a smooth potential due to the long range of the Coulomb force, so that a "three-point" approximation to $\nabla^2 W_C$ is adequate. However, W_Y varies relatively rapidly in space and a "five-point" approximation to $\nabla^2 W_Y$ is necessary (cf. Appendix A).

Given the values of W on the mesh boundaries (see below), the solution of Eqs. (C1) amounts to the inversion of a sparse matrix of dimensionality equal to the number of mesh points. It is not possible to invert directly and exactly such a large matrix. We therefore use an iterative method for solving Eqs. (C1) which constructs successive approximations to the solutions and continues the iteration process until sufficient precision is achieved. These methods have the added advantage that the potentials at the previous time step are excellent starting points for the iteration procedures. Recently an old and rediscovered method, the conjugate gradient method³¹ (CGM) has proven to be more rapid than the conventional successive over-relaxation methods or the alternating direction methods.³² We shall present the CGM for the Poisson equation and discuss briefly the precision achieved. The transposition to the Helmholtz problem is straightforward.

Our iterative scheme is a slight modification of

that proposed in Ref. 33. At the beginning of the time evolution we start with a first guess that the potential $W_C^{(0)}(\vec{r})$ is identically zero. Here, the upper index labels the number of iterations performed with the CGM method. At the following time steps we use as a starting point of the CGM the last computed value of $W_C(\vec{r})$. The calculation of the boundary conditions is discussed at the end of this Appendix. In order to begin the iterative scheme we need two additional vectors, $Z^{(0)}$ and $P^{(0)}$:

$$\begin{aligned} Z^{(0)} &= -[2\pi e^2 \rho(\vec{r}) + \nabla^2 W_C^{(0)}(\vec{r})], \\ P^{(0)} &= Z^{(0)}. \end{aligned} \quad (C2)$$

The iterative scheme which, in order to save computational time introduces an additional vector T and two scalars A and C , is then

$$T^{(k+1)} = \nabla^2 P^{(k)}, \quad (C3a)$$

$$A^{(k+1)} = (\vec{Z}^{(k)} \cdot Z^{(k)}) / (\vec{Z}^{(k)} \cdot T^{(k+1)}), \quad (C3b)$$

$$W_C^{(k+1)} = W_C^{(k)} + A^{(k+1)} P^{(k)}, \quad (C3c)$$

$$Z^{(k+1)} = Z^{(k)} - A^{(k+1)} T^{(k+1)}, \quad (C3d)$$

$$C^{(k+1)} = (\vec{Z}^{(k+1)} \cdot Z^{(k+1)}) / (\vec{Z}^{(k)} \cdot Z^{(k)}), \quad (C3e)$$

$$P^{(k+1)} = Z^{(k+1)} + C^{(k+1)} P^{(k)}. \quad (C3f)$$

In formulas (C3a)–(C3f) the symbol $(\vec{Z} \cdot T)$ is the scalar product of the two vectors Z and T . The method, in addition to its rapidity, provides a natural way to check the convergence. One can show that

$$Z^{(k)} = -[2\pi e^2 \rho(\vec{r}) + \nabla^2 W_C^{(k)}(\vec{r})] \quad (C4)$$

so that the norm of this vector is a measure of the remaining inaccuracy of $W_C^{(k)}(\vec{r})$. In our calculation we required this norm to be less than 10^{-10} .

The solution of both Eqs. (C1) requires a knowledge of the potential boundary conditions. We have assumed that the Yukawa potential is zero at the mesh boundaries. Because of the short Yukawa range ($a \approx 0.5$ fm), this assumption is valid if there is no appreciable density within about 1 fm of the boundaries. When the system approaches the mesh edges, this boundary condition results in a repulsive image potential and destroys the conservation of the total energy. We have therefore used this phenomenon as a signal for spurious effects from the mesh edges and have stopped the calculation when the total energy was not conserved to within a precision of about 1 MeV.

The long range of the Coulomb potential forces an explicit evaluation of W_C at the mesh boundaries. Indeed, setting the boundary conditions to zero would result in some 20% error in the Coulomb energy for the box dimensions used in our calculations. One possibility for evaluating the

boundary conditions for W_C is to evaluate Eq. (8c) at selected points on the box faces by means of Simpson's rule and then to compute the remaining boundary conditions by polynomial interpolation. This procedure requires relatively many sweeps of the mesh, but need only be carried out every 3 or 4 time steps. However, a far simpler procedure which is just as accurate is to perform a multipole expansion of the Coulomb potential.

If we assume that the system is always separated into two fragments in the way used to define the R coordinate in Sec. V, then the multipole moments of the fragments through order three are sufficient to give the required accuracy. This method has the additional advantage that it makes use of information which is interesting and would have been computed anyway, the lower multipole moments of the total system and of the fragments.

*Supported in part by the National Science Foundation (PHY76-83685) at Caltech.

†Permanent address: Division de Physique Theorique, Institut de Physique Nucleaire, BP No. 1, 91406 Orsay, France.

‡Alfred P. Sloan Foundation Fellow.

§This work was performed under the auspices of U. S. Energy Research and Development Administration under Contract No. W-7405-Eng-48.

¹P. A. M. Dirac, Proc. Camb. Phil. Soc. 26, 376 (1930).

²D. J. Thouless and J. G. Valatin, Nucl. Phys. 31, 11 (1962); D. J. Thouless, Nucl. Phys. 21, 225 (1961).

³M. Baranger, in *Cargèse Lectures in Theoretical Physics*, 1962, edited by M. Levy (Benjamin, New York, 1963).

⁴M. Baranger, J. Phys. (Paris) 33, C5-61 (1972); M. Baranger and M. Veneroni (unpublished).

⁵F. M. H. Villars, in *Dynamic Structure of Nuclear States*, edited by D. J. Rowe *et al.* (Univ. of Toronto Press, Toronto, 1972), p. 3.

⁶D. M. Brink, M. J. Giannoni, and M. Veneroni, Nucl. Phys. A258, 237 (1976).

⁷A. K. Kerman and S. E. Koonin, Ann. Phys. (N.Y.) 100, 332 (1976).

⁸Y. M. Engel, D. M. Brink, K. Goeke, S. J. Krieger, and D. Vautherin, Nucl. Phys. A249, 215 (1975).

⁹P. Bonche, S. E. Koonin, and J. W. Negele, Phys. Rev. C 13, 1226 (1976).

¹⁰R. Y. Cusson and J. Maruhn, Phys. Lett. 62B, 134 (1976); J. Maruhn and R. Y. Cusson, Nucl. Phys. A270, 437 (1967).

¹¹S. E. Koonin, Phys. Lett. 61B, 227 (1976).

¹²S. E. Koonin, K. T. R. Davies, V. Maruhn-Rezwani, H. Feldmeier, S. J. Krieger, and J. W. Negele, Phys. Rev. C 15, 1359 (1977).

¹³V. Maruhn-Rezwani, K. T. R. Davies, and S. E. Koonin, Phys. Lett. 67B, 134 (1977).

¹⁴P. Bonche, Proceedings of the Workshop IV on Gross Properties of Nuclei and Nuclear Excitations, Hirschegg, Austria, 1976 (unpublished).

¹⁵R. Y. Cusson, R. K. Smith, and J. Maruhn, Phys. Rev. Lett. 36, 1166 (1976).

¹⁶R. Y. Cusson, J. A. Maruhn, and H. W. Meldner, Oak Ridge National Laboratory Report, April, 1977 (unpublished).

¹⁷A. K. Kerman, in Proceedings of the International School of Physics, "Enrico Fermi," Varenna, 1976

(unpublished).

¹⁸P. Bonche, Proceedings of the Caen Conference on Heavy Ions, Caen, 1976 (unpublished).

¹⁹P. Bonche, B. Grammaticos, and S. E. Koonin, Phys. Rev. C 17, 1700 (1978), following paper.

²⁰V. M. Strutinsky, Nucl. Phys. A95, 420 (1967); A122, 1 (1968); M. Brack, International School of Nuclear Physics, Predial, Romania, 1974 (unpublished); V. M. Strutinsky, Nucl. Phys. A218, 169 (1974).

²¹W. J. Swiatecki, LBL Report No. 4296 (unpublished), presented at the International School Seminar on Reactions of Heavy Ions with Nuclei and Synthesis of New Elements, Dubna, USSR, 1975 (unpublished).

²²C. Y. Wong, J. A. Maruhn, and T. A. Welton, Nucl. Phys. A256, 469 (1975); Phys. Lett. 66B, 19 (1977).

²³M. J. Giannoni, D. Vautherin, M. Veneroni, and D. M. Brink, Phys. Lett. 63B, 8 (1976).

²⁴D. Vautherin, Comptes rendus de la troisieme session d'etudes biennale de la Toussuire, edited by El. Baz, 1975 (unpublished).

²⁵M. L. Goldberger and K. M. Watson, *Collision Theory* (Wiley, New York, 1964), Chap. 3.

²⁶See, for example, M. A. Preston and R. K. Bhaduri, *Structure of the Nucleus* (Addison-Wesley, Reading, Mass., 1975), p. 357; A. Bohr and B. R. Mottelson, *Nuclear Structure II* (Benjamin, New York, 1975), p. 692.

²⁷H. Flocard, Phys. Lett. 49B, 129 (1974).

²⁸P. Sperr, S. Vigdor, Y. Eisen, W. Henning, D. G. Kovar, T. R. Ophel, and B. Zeidman, Phys. Rev. Lett. 36, 405 (1976); P. Sperr, T. H. Braid, Y. Eisen, D. G. Kovar, F. W. Prosser, Jr., J. P. Schiffer, S. L. Tabor, and S. Vigdor, *ibid.* 37, 321 (1976); C. Gaarde *et al.* (unpublished).

²⁹M. Abramowitz and I. Stegun, *Handbook of Mathematical Functions* (National Bureau of Standards, Washington, D. C., 1965), p. 884.

³⁰A. R. Mitchell, *Computational Methods in Partial Differential Equations* (Wiley, New York, 1965).

³¹J. Reid, SIAM J. Num. Anal. 9, 325 (1972).

³²R. Varga, *Matrix Interactive Analysis* (Prentice-Hall, Englewood Cliffs, 1962), p. 273.

³³P. Concus, G. H. Golub, and D. P. O'Leary, *Sparse Matrix Computations*, edited by J. R. Bunch and D. J. Rose (Academic, New York, 1976); P. Concus, G. H. Golub, and C. W. Nielson, SIAM J. Num. Anal. 7, 627 (1970).

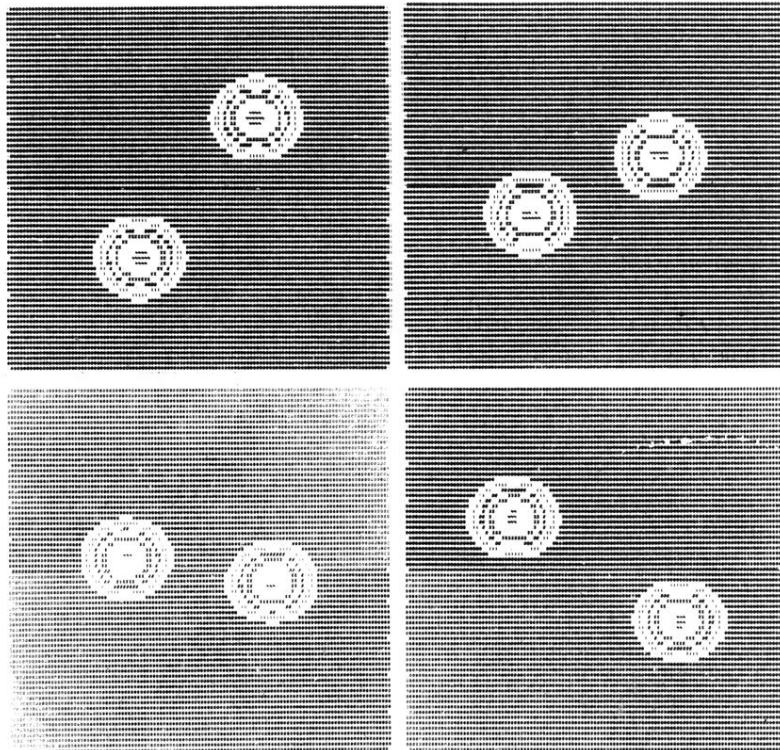


FIG. 1. Contour lines of the density integrated over the coordinate normal to the scattering plane for an $^{16}\text{O}+^{16}\text{O}$ collision at $E_{1\text{ab}}=105$ MeV and incident angular momentum $L=40\hbar$. The time interval between two pictures is 2×10^{-22} sec.

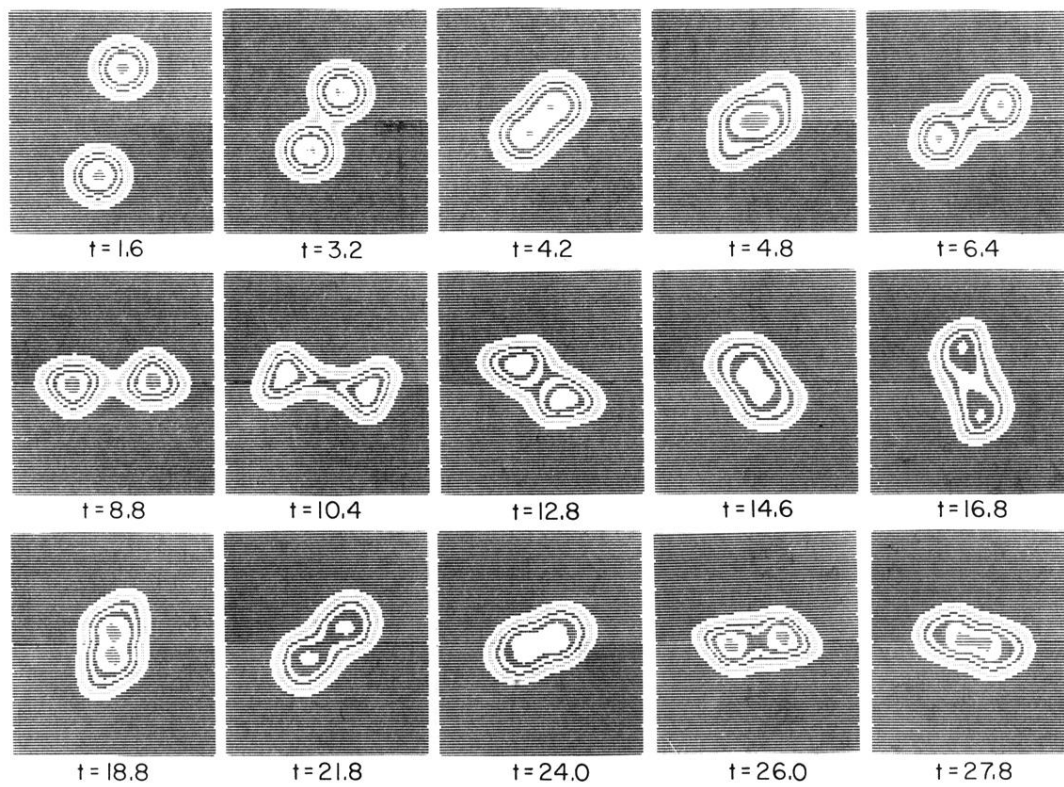


FIG. 2. Contour lines of the density integrated over the coordinate normal to the scattering plane for an $^{16}\text{O} + ^{16}\text{O}$ collision at $E_{\text{lab}} = 105$ MeV and incident angular momentum $L = 13\hbar$. The times t are given in units of 10^{-22} sec.

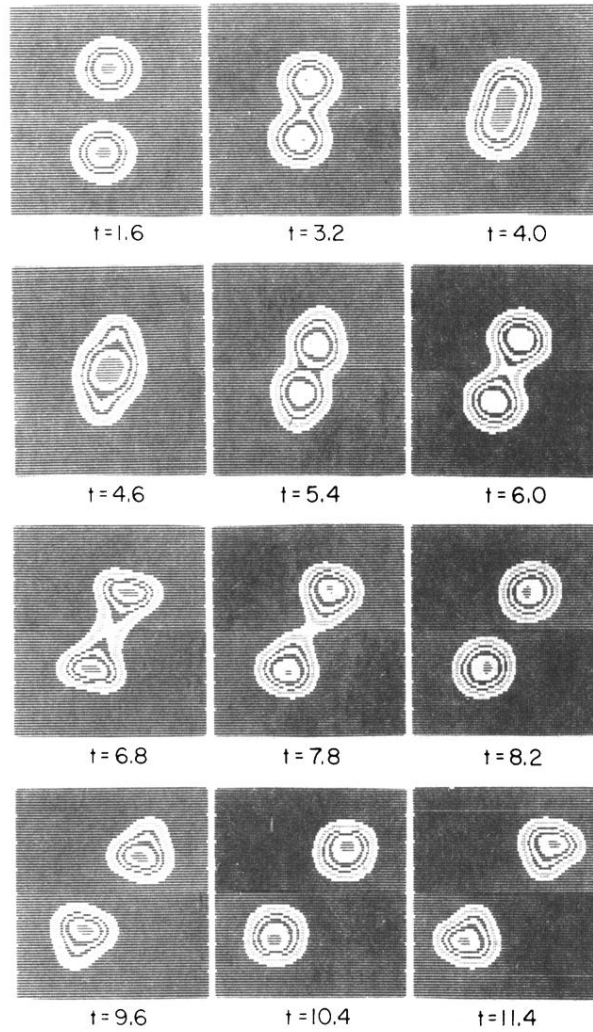


FIG. 3. Contour lines of the density integrated over the coordinate normal to the scattering plane for an $^{16}\text{O} + ^{16}\text{O}$ collision at $E_{\text{lab}} = 105$ MeV and incident angular momentum $L = 5\hbar$. The times t are given in units of 10^{-22} sec.

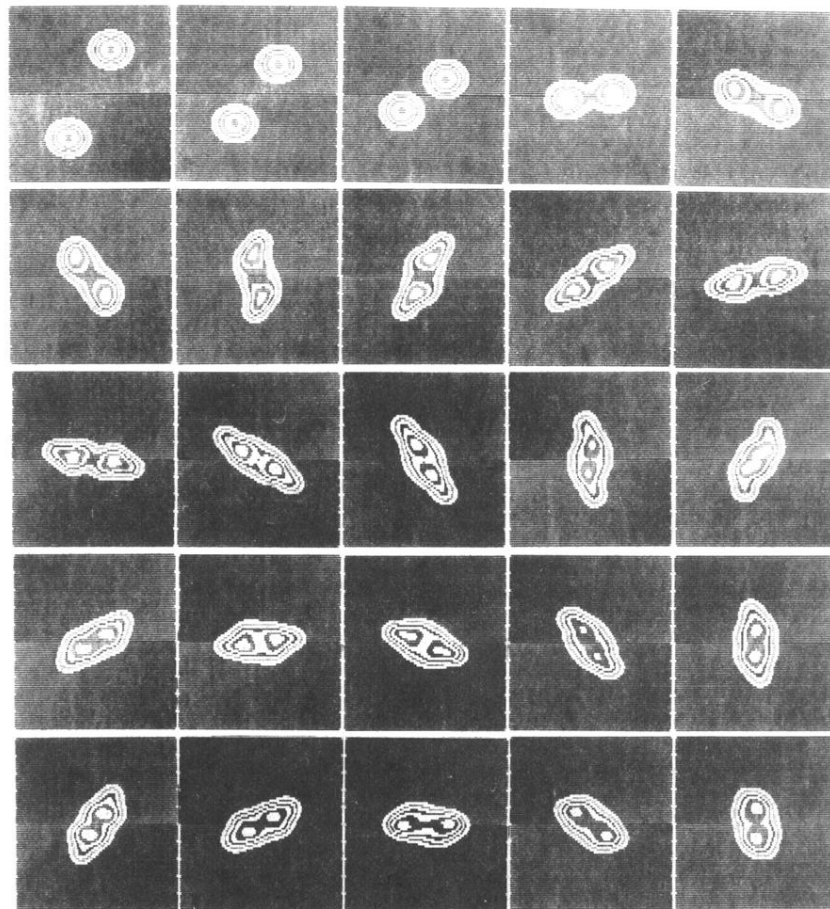


FIG. 7. Contour lines of the density integrated over the coordinate normal to the scattering plane for an $^{16}\text{O}+^{16}\text{O}$ collision at $E_{\text{lab}}=192$ MeV and incident angular momentum $L=42\hbar$. The time interval between two pictures is 10^{-22} sec.